

Gate tunable anomalous Hall effect at (111) LaAlO₃/SrTiO₃ interface

M. Trama,^{1,2,*} V. Cataudella,^{3,4} C. A. Perroni,^{3,4} F. Romeo,¹ and R. Citro^{1,2,†}

¹*Physics Department "E.R. Caianiello", Università degli studi di Salerno, Via Giovanni Paolo II, 132, I-84084 Fisciano (Sa), Italy*

²*INFN - Sezione di Napoli, Complesso Univ. Monte S. Angelo, I-80126 Napoli, Italy*

³*Physics Department "Ettore Pancini", Università degli studi di Napoli "Federico II", Complesso Univ. Monte S. Angelo, Via Cintia, I-80126 Napoli, Italy*

⁴*CNR-SPIN Napoli Unit, Complesso Univ. Monte S. Angelo, Via Cintia, I-80126 Napoli, Italy*

We present the theoretical prediction of a gate tunable anomalous Hall effect (AHE) in an oxide interface as a hallmark of spin-orbit coupling. The observed AHE at low-temperatures in the presence of an external magnetic field emerges from a complex structure of the Berry curvature of the electrons on the Fermi surface and strongly depends on the orbital character of the occupied bands. A detailed picture of the results comes from a multiband low-energy model with a generalized Rashba interaction that supports characteristic out-of-plane spin and orbital textures. We discuss strategies for optimizing the intrinsic AHE in (111) SrTiO₃ heterostructure interfaces.

The anomalous Hall effect (AHE), a hallmark of broken time-reversal symmetry and spin-orbit coupling, has long been an intriguing even though controversial subject. In fact, some of the theories explain the AHE as an effect of the skew scattering [1] or side jump mechanism [2] and goes under the name of *extrinsic* AHE. Moreover, several studies have pointed out the intrinsic origin of the AHE, related to the Berry curvature of the quasiparticles on the Fermi surface [3–8]: the mobile charge carriers gain a transverse momentum due to a magnetic polarization coming from the Berry curvature of the occupied Bloch wave functions (cfr. Eq. 6). The corresponding Hall voltage, i.e. anomalous Hall component, can be observed as an additional contribution in the Hall measurements, superposed on the ordinary Hall effect. This Berry scenario of the AHE has recently attracted interest for its dissipationless and topological nature. However, up to now, the experimental realization of AHE in non-magnetic systems and in the moderately dirty limit remains elusive. In this Letter we propose oxide interfaces—artificially created structures involving transition-metal oxide compounds— as a platform for intrinsic AHE. Here the large spin-orbit coupling (SOC) and the multi-orbital character of the bands enrich the variety of emergent SOC phenomena [9], like the generation and control of spin and orbital textures [10] at the origin of the AHE. One of the prototypes among these oxide interfaces is the LaAlO₃/SrTiO₃ (LAO/STO), whose Rashba interaction allows the manipulation of the spin of the electrons through an applied electric field [11]. Among such interfaces, recent attention has been devoted to the (111) LAO/STO interface, whose trigonal geometry leads to exotic behaviours, including analogy with graphene in the conducting state [12, 13] and anisotropic magnetic transport both in normal and superconducting state [14, 15].

Here, we predict a gate tunable intrinsic anomalous Hall conductivity (AHC) in (111) LAO/STO coming from an out-of-plane spin and orbital texture [16] associated with a non-vanishing Berry curvature in the presence of an in- and out-of-plane magnetic field. We show that this behavior arises from a generalized Rashba coupling involving the total angular momentum of the bands, and construct an effective Hamiltonian for the low-filling region, underlining the strong orbital character of the Rashba interaction in the (111) direction. This behavior has not been predicted in the more common (001) LAO/STO, establishing the (111) STO interfaces among the reconfigurable platforms for spin-orbitronics [17].

We develop a tight-binding model of the electrons at the interface occupying the t_{2g} orbitals of a bilayer of Ti atoms in STO [18]. The Ti lattice projected along the (111) direction is a honeycomb lattice (see Fig. 1(a-b)). The Hamiltonian originating from the three t_{2g} orbitals of the Ti-atoms in the α and β layers reads [13, 19, 20]

$$H = H_{\text{TB}}(t_D, t_I) + H_{\text{SOC}}(\lambda) + H_{\text{TRI}}(\Delta) + H_v(v), \quad (1)$$

where H_{TB} is the hopping Hamiltonian depending on the direct and indirect hopping parameters, t_D and t_I , respectively; H_{SOC} is the atomic SOC with strength λ [21]; H_{TRI} describes the strain at the interface, whose origin is attributed to contraction or dilatation of the crystalline planes along the (111) direction. We will refer to this term as the trigonal crystal field, parametrized by the coupling Δ . Finally, the last term H_v describes an electric field in the (111) direction, orthogonal to the interface, breaking reflection symmetry. Differently from previous studies [20, 21], we treat the effect of the electric field \vec{E} on the orbitals perturbatively. In particular, following Ref. [22], we consider that \vec{E} induces an hybridization of the atomic d orbitals of the STO from $|d\rangle$ to $|d'\rangle = c_1|p\rangle + c_2|d\rangle + c_3|f\rangle$, with $|x\rangle$ the atomic orbital x , leading to renormalized hopping terms odd in lattice momentum \vec{k} . In addition to the previous terms in H , one can consider the Hamiltonian $H_{\text{H}}(U, U', J)$ which describes the intra-orbital and inter-orbital Hubbard and

* mtrama@unisa.it

† rocitro@unisa.it

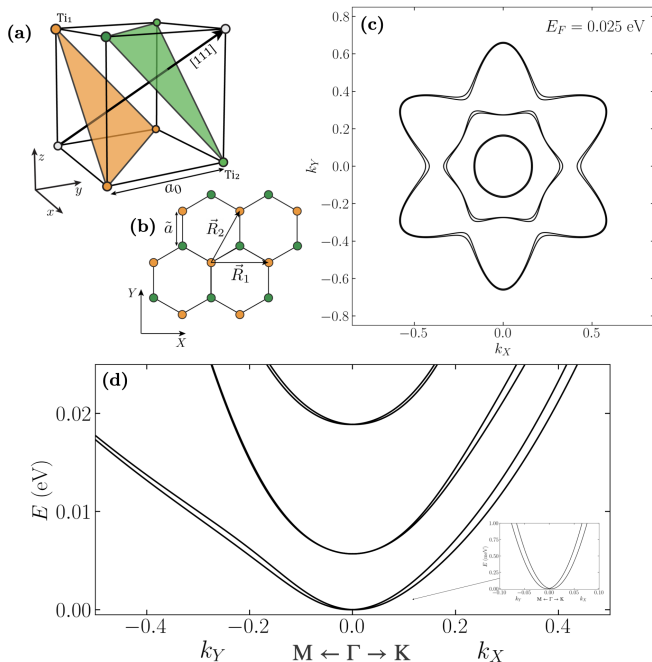


Figure 1. (a) Ti atoms in STO lattice, whose reticular constant is $a_0 = 0.3905$ nm. The orange and green dots represent atoms belonging to two non-equivalent planes. (b) Projection of the two non-equivalent planes of Ti over the (111) plane with our choice of primitive vectors \vec{R}_1 and \vec{R}_2 and $\tilde{a} = \sqrt{2/3}a_0$. (c) Fermi surface for the Fermi energy $E_F = 0.025$ eV. (d) Band structure along two different directions in the Brillouin zone. The detail of the splitting at low fillings of the first doublet, exhibiting the typical Rashba behaviour, is depicted in the inset. Panels (c) and (d) are evaluated at $\vec{B} = 0$.

Hund's interaction [23]. For the regime of small interaction parameters we have verified that its effect is simply a renormalization of the chemical potential [19]. Moreover, one can include the effect of tetragonal distortion at low temperature [24] through a contribution H_ζ . The analysis of this contribution is given in the supplementary [19].

The full Hamiltonian leads to the band structure in Fig. 1(d), where a Rashba-like splitting appears in the lowest band due to the interplay between SOC and reflection symmetry breaking term. The splitting between the Kramers doublets, visible in the Fermi surface in Fig. 1(c), is consistent with previous results [25]. The behaviour for low filling can be recovered by the effective Hamiltonian derived from a perturbative approach truncated at the order $\sim O(\vec{k}^2)$ [19]:

$$H_{\text{eff}}(\vec{k}) = \sum_i \mathcal{E}_i(\vec{k})(\mathbb{1} - L_i^2) - \frac{\lambda}{2} \hat{L} \cdot \hat{S} - \Delta L_{111}^2 + \mathcal{F}(\vec{k} \times \hat{L}) + E_0, \quad (2)$$

where $\mathcal{E}_i(\vec{k})$ is the renormalized band dispersion coming from the second order expansion, L_i and S_i are the i -th component of the orbital and spin angular momentum

operator for $L = 1$ and $S = 1/2$, respectively; the second term is a spin-orbit interaction; L_{111} is the projection of \vec{L} along the (111) direction and the second to last term is an orbital-Rashba interaction [26], whose coefficient \mathcal{F} is derived in [19]. We have verified that the effective Hamiltonian gives the same spectrum of Hamiltonian 1 up to $|\vec{k}| \sim 0.5$ (in unit of \tilde{a}) while all the results are obtained using the full Hamiltonian. In Eq. 2 a first signature of a generalized Rashba coupling appears, due to the term $(\vec{k} \times \hat{L})$. Near $\vec{k} = 0$, the Hamiltonian is dominated by atomic SOC, so we can use as a basis the eigenstates of $\vec{J} = \vec{S} + \vec{L}$. Evaluating the Hamiltonian over a multiplet of definite total angular momentum J , the effective Hamiltonian can be written as

$$H_{\text{eff}}(|\vec{k}| \sim 0) = -\tilde{\Delta} J_{111}^2 + \tilde{\mathcal{F}}(\vec{k} \times \hat{J}) + \sum_i \mathcal{E}_i(\vec{k})(\nu \mathbb{1} - \tau J_i^2), \quad (3)$$

where $\tilde{\Delta}$, $\tilde{\mathcal{F}}$, ν , and τ are rescaled parameters [19] and J_{111} is the projection of the total angular momentum in the (111) direction. The SOC splits the bands in two groups: four states of lower energy with $J = 3/2$ and a doublet of $J = 1/2$ at higher energy. Since the trigonal crystal field splits the states according to their value of \vec{J} along the (111) direction, the first doublet in Fig. 1 has $J_{111} = \pm 1/2$, while the second doublet has $J_{111} = 3/2$. For this reason the splitting of the second doublet depicted in Fig 1(d) is not linear in the wavevector \vec{k} , as for the canonical Rashba interaction, but cubic [27]. We also note that Eq. 34 is not valid for a trigonal crystal field comparable or even larger than the SOC, since the eigenstates of total angular momentum are not anymore a reasonable approximation to the real eigenstates of the problem.

The interplay between spin and orbital angular momentum causes peculiar patterns shown in Fig. 2 (see Supplementary [19] for the total angular momentum patterns). For the first two bands the pattern is Rashba-like with a spin amplitude changing with \vec{k} . The third and the fourth bands have a Rashba-like vortex near the Γ point, replaced by six secondary vortices at larger \vec{k} .

If we add to the Hamiltonian 1 a Zeeman term H_B of the form

$$H_B = -\mu_B \vec{B} \cdot (\hat{L} + 2\hat{S}) \quad (4)$$

the time-reversal symmetry of the model is broken. This is associated to a non-vanishing out-of-plane Berry curvature. To evaluate its effect on the intrinsic AHE, we employ a semi-classical approach based on the Boltzmann equations within the time-relaxation approximation. In the presence of a small in-plane electric field \vec{E}_{ext} , the electron group velocity is given by:

$$\vec{v}_g = \frac{1}{\hbar} \frac{\partial \epsilon}{\partial \vec{k}} - \frac{e}{\hbar} \vec{E}_{\text{ext}} \times \vec{\Omega} \quad (5)$$

where the former term is the standard dynamical contribution, while the latter is the geometric contribution

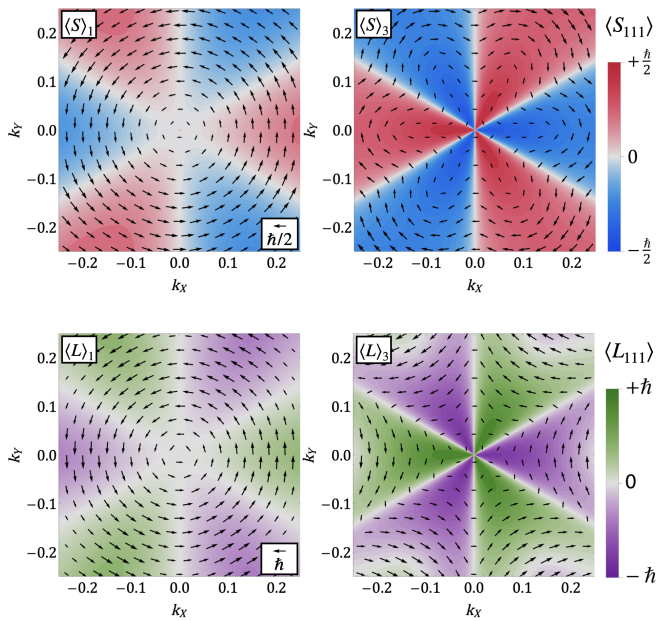


Figure 2. In- and out-of-plane spin and angular momentum modulation for the first and the third band. The second and the fourth are specular to the ones shown. The in-plane patterns are represented by the arrows and are obtained by computing the mean value of the spin (orbital) components $S_{[\bar{1}10]}$ ($L_{[\bar{1}10]}$) and the $S_{[\bar{1}\bar{1}2]}$ ($L_{[\bar{1}\bar{1}0]}$) over the eigenstates of the chosen band. The colours indicate the out-of-plane modulation.

connected to the Berry curvature $\vec{\Omega}$. This term originates the intrinsic AHE, mainly discussed in ferromagnetic systems [28]:

$$\sigma_{XY}^{\text{AH}} = -\frac{e^2}{\hbar} \sum_{n \text{ occ}} \int_{BZ} \Omega_{n\vec{k}} f_{th,\vec{k}}(T) \frac{d^2\vec{k}}{(2\pi)^2}, \quad (6)$$

where f_{th} is the Fermi distribution at temperature T (where X and Y are the $(\bar{1}10)$ and the $(\bar{1}\bar{1}2)$ directions) and $\Omega_{n\vec{k}}$ refers to the (111) component of the Berry curvature of the n -th band, the only non-vanishing component for a 2D system. The magnetic field changes the eigenstates and therefore enters implicitly the Berry curvature. The intrinsic AHE occurs in the moderately dirty regime in which AHC becomes non-dissipative, i.e. independent of the scattering rate [29]. In this regime, the Berry phase of the quasiparticles on the Fermi surface acts as an effective magnetic field generating a transverse momentum. In the dirty regime, however, the extrinsic AHC is directly proportional to the longitudinal conductivity. The extrinsic to intrinsic crossover occurs when the scattering rate becomes comparable to Fermi energy [30]. In general, insurgence of point defects, such as oxygen vacancies and intermixed cations at LAO/STO interfaces can be controlled e.g. by using an amorphous WO_3 overlayer to obtain an increased electron mobility [31]. Thus the intrinsic contribution can be made evident. Our main result is shown in Fig. 3 where we plot the AHC

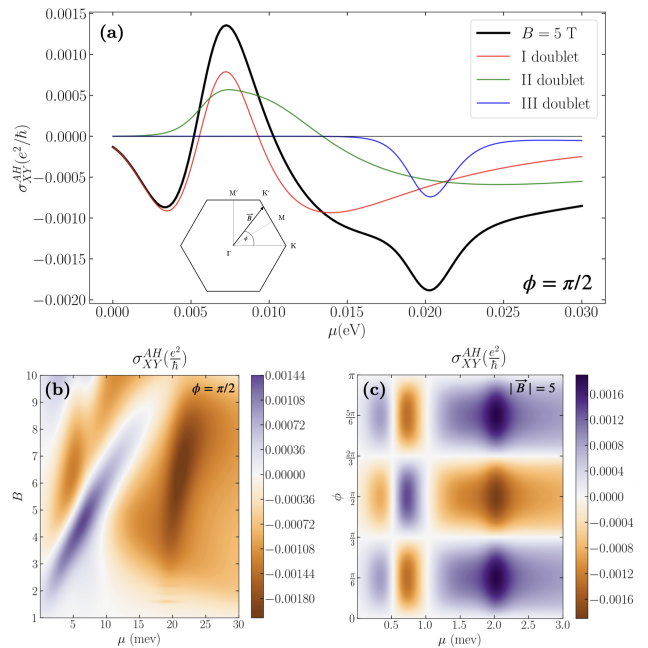


Figure 3. (a) AHC as a function of the chemical potential μ for an in-plane magnetic field $|B|=5$ T, with an in-plane angle $\phi = \pi/2$ at a temperature $T = 10$ K. The colors indicate the sum of the contributions over two specific bands. (b) AHC as a function of μ and for different values of $|\vec{B}|$ with $\phi = \pi/2$ and $T = 10$ K. (c) AHC as a function of μ for different values of ϕ at $|\vec{B}|=5$ T and $T = 10$ K.

as a function of the chemical potential in the presence of an *in-plane* magnetic field. First, in panel (a) we observe a highly non-linear behavior as a function of the gate voltage. We observe a modulation of the conductance which comes from the sum of the three contributions associated to the doublets of the electronic band structure in Fig. 1(d). In panel (b) we show that this behaviour extends over a wide range of magnetic field magnitudes. In panel (c) we show the periodic behaviour of the AHC by varying the direction of the in-plane magnetic field. The pattern reflects the C_{3v} symmetry of the system; the conductance vanishes when the magnetic field is aligned along the high symmetry lines $\Gamma\text{K}(\Gamma\text{K}')$ [19]. The origin of the non-linearity and strong modulation with applied magnetic field stems from two major ingredients: the almost-degenerate multiband structure and the complex topological structure of the Berry curvature.

To discuss the relation between the AHC and Berry curvature, we show the AHC $\sigma_{XY}^{\text{AH}}(\mu)$ as a function of the chemical potential for an *out-of-plane* magnetic field in Fig. 4. In this case the magnetic field is aligned along the (111) direction preserving J_{111} , simplifying the problem. The conductivity has a non-linear behavior, as in the case of an in-plane magnetic field, and exhibits more than one dip by varying the chemical potential. Differently from the first dip, the second one is very sensitive to the magnitude of the magnetic field and progressively

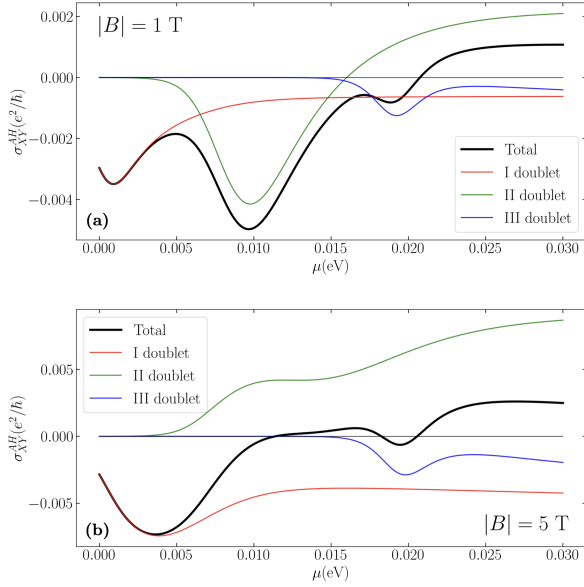


Figure 4. AHC as a function of the chemical potential μ when \vec{B} is out-of-plane for (a) $|\vec{B}| = 1$ T and (b) $|\vec{B}| = 5$ T (the temperature is fixed to $T = 10$ K). The colored lines represent the contributions from the specific bands.

raises on increasing the magnetic field, until it completely disappears. This can be qualitatively explained by the stronger dependence of the second doublet band splitting on the magnetic field due to its $J = 3/2$ character. This is in contrast with the first and third doublet whose splitting is dominated by the Rashba term. This permits us to conclude that the AHE can be optimized by a gate voltage, at a fixed magnetic field, by moving it close to the second doublet.

The dips in the conductivity appears when the Fermi surface encircles one or more peaks of the Berry curvature (see Fig. 5). We observe that the sum of the Berry curvatures of the two bands within the same doublet is typically small, due to partial cancellation (which would be exact under time-reversal symmetry). The splitting of the bands of one doublet can be taken as a small parameter, $\varepsilon_{2\vec{k}} = \varepsilon_{1\vec{k}} + \delta\varepsilon_{\vec{k}}$. Thus the Fermi distribution, namely the Heaviside function at zero temperature, is expanded as $\Theta(\mu - \varepsilon_{1\vec{k}} - \delta\varepsilon_{\vec{k}}) \sim \Theta(\mu - \varepsilon_{1\vec{k}}) + \delta(\mu - \varepsilon_{1\vec{k}})\delta\varepsilon_{\vec{k}}$. Since $\Omega_2 = -\Omega_1 + \delta\Omega$, the contribution of a single doublet to the AHC is

$$\sigma_{XY}^{\text{AH},I} \sim - \int_{BZ} [\Omega_{1\vec{k}}\delta(\mu - \varepsilon_{1\vec{k}})\delta\varepsilon_{\vec{k}} + \delta\Omega\Theta(\mu - \varepsilon_{1\vec{k}})] \frac{d^2\vec{k}}{(2\pi)^2}, \quad (7)$$

in units of $\frac{e^2}{h}$, where we can identify the first term as a ring contribution and the second one as an area contribution. The ring contribution is maximum where the curvature is peaked, and leads to the peaks in the AHC; at higher fillings, the area contribution saturates to a constant value and dominates, as can be seen from Fig. 4. The change in sign of the conductance is a consequence

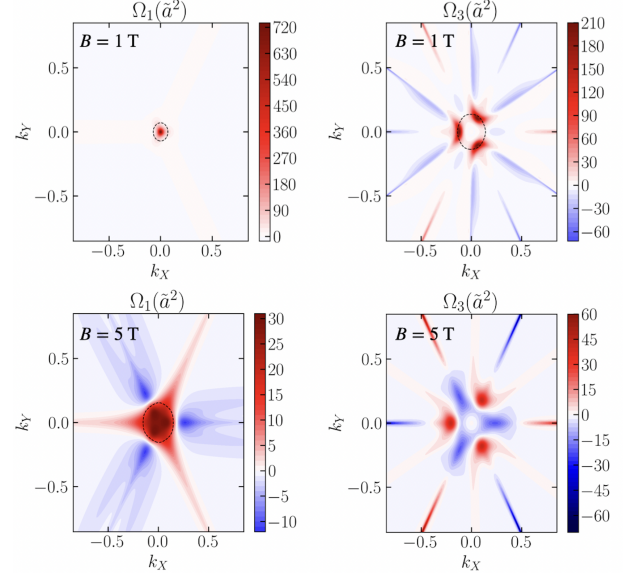


Figure 5. Berry curvatures of the first and the third band at $|\vec{B}| = 1$ T and $|\vec{B}| = 5$ T. The figures shows a change of the topology of the Berry curvature of a fixed band increasing the magnetic field leading to a non trivial behaviour of the conductance.

of the competition of the different doublets contribution: this reflects the importance of the multi-orbital character of the interface for the tunability of the AHE. Note that the sign change disappears with increasing temperature (in any case above 30 K) or with including the effects of strong Coulomb electron-electron correlations (for more details, see Supplementary [19]).

The out-of-plane magnetic field also gives a conventional Hall conductance which can hinder the anomalous one since its order of magnitude has been verified to be of the order of $10^4 e^2/h$ when $|\vec{B}| = 5$ T and it cannot be easily subtracted by the total conductance experimentally since it is not linear. This is due to the multiband structure and the presence of the Berry curvature which modifies the element of volume of the phase-space for each band [32]. Therefore the major evidence of AHE comes from an in-plane magnetic field, since the results shown in Fig. 3 are not affected by the conventional contribution.

Discussion and conclusions. We have pointed out and discussed a gate tunable AHE in an oxides interface. The multiband structure of (111) LAO/STO is characterized by a strong near-degeneracy at low fillings and momenta, as well as a strong dependence of the orbital angular momentum on the filling. The combination of these features is responsible for a generalized Rashba coupling in an external electric field. The SOC, which can be quite large in oxides, naturally converts this coupling into a novel Rashba coupling to the total angular momentum. As a first consequence of this Rashba coupling here, we have shown the presence of a spin and angular momentum patterns in- and out-of-plane. Second, we have shown the

emergence of an AHC under broken time-reversal symmetry, due to a non-trivial topological Berry curvature, even for an in-plane magnetic field. Finally, the generalized Rashba coupling can strongly affect the behavior of these materials in the superconducting phase in analogy with the case of (001) LAO/STO interface [33, 34].

Our study on LAO/STO interface does not preclude the presence of such effects in other interfaces. The main requirement is the trigonal geometry and the quenching of the t_{2g} orbitals which is also found in $\text{K}\alpha\text{TiO}_3/\text{SrTiO}_3$ [35]. This work opens the way to a general study of the *spin-orbitronic* effects induced by the generalized Rashba coupling in novel interfaces and paves the way to its experimental verification via a gate tunable AHE.

Note added. Recently, we became aware of similar work carried out by first author E. Lesne et al. [36] observing the anomalous Hall effect in LAO/STO (111).

Acknowledgments. We thank A.Caviglia for insightful suggestions and discussions. C.A.P. acknowledges support from Italy's MIUR PRIN project TOP-SPIN (Grant No. PRIN 20177SL7HC), C.A.P. and R. C. from project QUANTOX (QUANTum Technologies with 2D-OXides) of QuantERA ERA-NET Cofund in Quantum Technologies (Grant Agreement No. 731473) implemented within the European Union's Horizon 2020 Programme.

Appendix A THE TIGHT-BINDING MODEL

The effective 2D single particle Hamiltonian originating from the three t_{2g} orbitals of the Ti-atoms in the bilayer reads [13, 20]

$$H = H_{\text{TB}}(t_D, t_I) + H_{\text{SOC}}(\lambda) + H_{\text{TRI}}(\Delta) + H_v(v), \quad (8)$$

where H_{TB} is the hopping Hamiltonian which in \vec{k} -space can be written as:

$$H_{\text{TB}} = \sum_{\vec{k}} \sum_{i, \alpha, \beta, \sigma} t_i^{\alpha\beta}(t_D, t_I, \vec{k}) d_{i\alpha\sigma, \vec{k}}^\dagger d_{i\beta\sigma, \vec{k}}, \quad (9)$$

where $d_{i\alpha\sigma, \vec{k}}$ is the annihilation operator of the electron with 2D dimensionless quasi-momentum $\vec{k} = \tilde{a}\vec{K}$, where \vec{K} is the quasi-momentum, occupying the orbital $i = xy, yz, zx$ belonging to the layer $\alpha, \beta = T_{i_1}, T_{i_2}$ and of spin $\sigma = \pm 1/2$. The matrix $t_i^{\alpha\beta}(t_D, t_I, \vec{k})$ includes the nearest-neighbour hopping parameters which have been separated in direct t_D and indirect t_I contribution, fixed to the values $t_D = 0.5$ eV and $t_I = 0.04$ eV [13].

H_{SO} is the atomic SOC coupling, which has the following expression

$$H_{\text{SOC}} = \frac{\lambda}{2} \sum_{\vec{k}} \sum_{ijk, \alpha, \sigma, \sigma'} i\varepsilon_{ijk} d_{i\alpha\sigma, \vec{k}}^\dagger \sigma_{\sigma\sigma'}^k d_{j\alpha\sigma', \vec{k}} \quad (10)$$

where ε_{ijk} is the Levi-Civita tensor, and σ^k are the Pauli matrices. We fix the SOC coupling $\lambda = 0.01$ eV, as a typical order of magnitude [21].

H_{TRI} takes into account the strain at the interface along the (111) direction. The physical origin of this strain is the possible contraction or dilatation of the crystalline planes along the (111) direction. This coupling has the form [37]

$$H_{\text{TRI}} = \frac{\Delta}{2} \sum_{\vec{k}} \sum_{i \neq j, \alpha, \sigma} d_{i\alpha\sigma, \vec{k}}^\dagger d_{j\alpha\sigma, \vec{k}}. \quad (11)$$

In the following we will refer to this term as the trigonal crystal field. We fix $\Delta = -0.005$ eV as reported in [38]. Finally the last term H_v describes an electric field in the (111) direction, orthogonal to the interface, which breaks the reflection symmetry. Following the calculation in [22] we take into account the fact that \vec{E} induces an hybridization of the atomic d orbitals of the STO from $|d\rangle$ to $|d'\rangle = c_1|p\rangle + c_2|d\rangle + c_3|f\rangle$ leading to renormalized hopping terms which are odd in \vec{k} (see Section 2). The Hamiltonian H_v can thus be written as

$$H_v = \frac{v}{2} \sum_{i, \alpha, \sigma, \vec{k}} \xi_\alpha d_{i\alpha\sigma, \vec{k}}^\dagger d_{i\alpha\sigma, \vec{k}} + \sum_{\vec{k}} \sum_{ij, \alpha, \beta, \sigma} h_{ij, \vec{k}}^{\alpha\beta}(v) d_{i\alpha\sigma, \vec{k}}^\dagger d_{j\beta\sigma, \vec{k}} \quad (12)$$

where $\xi_{T_{i_1}/T_{i_2}} = \pm 1$ and the expression of matrix elements $h_{ij, \vec{k}}^{\alpha\beta}(v)$ are obtained in the next section. The electric field has been fixed at the value $v = 0.2$ eV by comparison with the Rashba splitting evaluated in Ref. [21].

Appendix B DERIVATION OF THE RASHBA TERM

In this section we will derive the effective Rashba term originated from the combination of the SOC and the inversion symmetry breaking due to the electric field. Here we will first give some details of the calculation of the hopping elements originated from the modification of the orbital shape due to the electric field, and thus the matrix elements of the Hamiltonian 12. As we discussed in the main text, we follow the calculation in [22], which was referred to another geometry, therefore we will summarize the general idea and give explicitly the results applied to the (111) STO geometry.

We need to diagonalize the Hamiltonian $H = H_0 + \eta H_E$, where $H_0 = H_{\text{TB}} + H_{\text{SO}} + H_{\text{TRI}}$ in the real space, $H_E = -eE_j r_j$ where $\vec{E} = E_0(1, 1, 1)/\sqrt{3}$ and $\eta = 1$ is the small parameter of the perturbation expansion. The electric field can be considered as a small perturbation causing the atomic orbitals localized at the position \vec{R} to change in the form $|\phi_{\alpha\vec{R}}\rangle = |\phi_{\alpha\vec{R}}^0\rangle + \eta |\phi_{\alpha\vec{R}}^I\rangle$, where $|\phi_{\alpha\vec{R}}^0\rangle$ are the unperturbed atomic orbitals. The hamiltonian matrix to first order in η changes in the following way:

$$H_{\alpha\beta} = \langle \phi_{\alpha\vec{0}}^0 | H_0 | \phi_{\beta\vec{R}}^0 \rangle + \eta \langle \phi_{\alpha\vec{0}}^I | H_0 | \phi_{\beta\vec{R}}^0 \rangle + \eta \langle \phi_{\alpha\vec{0}}^0 | H_0 | \phi_{\beta\vec{R}}^I \rangle + \eta \langle \phi_{\alpha\vec{0}}^0 | H_E | \phi_{\beta\vec{R}}^0 \rangle + O(\eta^2). \quad (13)$$

The latest electrostatic term can be neglected since it couples the same orbital to different sites; this is due to the distance between neighbouring sites which causes the matrix elements of H_E to be exponentially suppressed. The modification of the atomic orbitals can be expressed as

$$\left| \phi_{\alpha\bar{R}}^I \right\rangle = \sum_{\beta \neq \alpha} \frac{\langle \phi_{\beta\bar{R}}^0 | H_E | \phi_{\alpha\bar{R}}^0 \rangle}{\epsilon_\alpha - \epsilon_\beta} \left| \phi_{\beta\bar{R}}^0 \right\rangle, \quad (14)$$

evaluated on the same site and where α runs over the d orbitals, while β runs over all the other orbitals; here ϵ_α are the on-site energies of the α -th orbital. We emphasize that the distortion of the orbitals is a completely local, on-site effect. The angular part of the matrix element in Eq. 14 can be expressed in terms of the Gaunt Coefficients using the spherical harmonics Y_m^l of the wavefunctions in Eq. 14

$$C_{lm,l'm',l''m''} = \int Y_m^l (Y_{m'}^{l'})^* Y_{m''}^{l''} d\Omega \quad (15)$$

in which Y_m^l comes from the electric field, $Y_{m''}^{l''}$ comes from $\left| \phi_{\alpha\bar{R}}^0 \right\rangle$, which is a d orbital with $l'' = 2$, and $Y_{m'}^{l'}$ comes from $\left| \phi_{\beta\bar{R}}^0 \right\rangle$. The coefficients vanish unless $l' = l'' \pm 1$, since $l = 1$.

The radial part of the matrix element is included in the following coefficient defined as

$$\eta_\beta = \frac{|e|\vec{E}|}{\epsilon_{3d} - \epsilon_\beta} \int R_{3d}(|\vec{r}|) |\vec{r}|^3 R_\beta(|\vec{r}|) d|\vec{r}|. \quad (16)$$

where $R_\beta(|\vec{r}|)$ is the radial part of the wavefunction.

One can compute the corrections to the t_{2g} states due to the perturbation obtaining¹

$$\left| d_{xy}^I \right\rangle = \frac{\eta_p}{\sqrt{15}} (|p_x\rangle + |p_y\rangle) + \frac{\eta_f}{\sqrt{7}} \left[\frac{2\sqrt{2}}{\sqrt{5}} (|f_{x^2y}\rangle + |f_{xy^2}\rangle) + |f_{xyz}\rangle \right]. \quad (17)$$

and obtaining $\left| d_{yz}^I \right\rangle$ and $\left| d_{zx}^I \right\rangle$ with cyclic permutations of x , y and z . It is worthwhile noticing that the η_f is small compared to η_p [22], so that in the following we will consider only the $|p_i\rangle$ corrections.

Now we can calculate the matrix elements $(\langle \phi_{\alpha\bar{0}}^I | H_0 | \phi_{\beta\bar{R}}^0 \rangle + \langle \phi_{\alpha\bar{0}}^0 | H_0 | \phi_{\beta\bar{R}}^I \rangle)$. Let us assume for the H_0 eigenstates the following notation in the expansion of the atomic orbitals expressed as a function of the quasi-momentum \vec{K} :

$$\left| \phi_{i\vec{K}}^{\text{Ti}\alpha} \right\rangle = |i_{\vec{K}}, \alpha\rangle = \frac{1}{\sqrt{N}} \sum_{\vec{r}} e^{-i\vec{K}\cdot\vec{r}} |i(\vec{r} - \vec{\delta}_\alpha)\rangle, \quad (18)$$

where we emphasized the fact that two non-equivalent Ti atoms in the same crystal cell are separated by a base vector, so that $\vec{\delta}_\alpha = \{(0,0), (0, -a_0)\} = \{\vec{0}, \vec{\delta}\}$ in the 2D space. To shorten the notation, we write the corrections of the d orbitals defined in Eq. 17 as

$$|d_i(\vec{r})^I\rangle = \mathcal{A}_{ij} |p_j(\vec{r})\rangle. \quad (19)$$

First of all, let us calculate these matrix elements over the nearest neighbour atoms, coupling the Ti atoms from different layers. Therefore we need to compute the following matrix elements

$$\begin{aligned} \left\langle d_{i,\vec{K}}^I, 1 \left| H_0 \right| d_{j,\vec{K}}, 2 \right\rangle + \left\langle d_{i,\vec{K}}, 1 \left| H_0 \right| d_{j,\vec{K}}^I, 2 \right\rangle &= \\ &= \sum_{\vec{a}} \mathcal{A}_{ik}^* \left\langle p_k(\vec{r}) \left| H_0 \right| d_j(\vec{r} - \vec{a} - \vec{\delta}) \right\rangle e^{-i\vec{K}\cdot\vec{a}} + \\ &+ \mathcal{A}_{jk} \left\langle d_i(\vec{r}) \left| H_0 \right| p_k(\vec{r} - \vec{a} - \vec{\delta}) \right\rangle e^{-i\vec{K}\cdot\vec{a}}, \end{aligned} \quad (20)$$

where \vec{a} are the vectors connecting the nearest neighbour elementary cells. For every \vec{a} we can associate a certain direction in terms of the 2D-dimensionless quasi-momentum $\vec{k} = (k_X, k_Y)$ via projection of the (111) plane:

¹ Notice that these corrections do not coincide with the ones presented in Ref. [22] because of the different orientation of the

electric field.

- for $\vec{a} = \vec{a}_x = a_0(1, 0, 0) \rightarrow \vec{K} \cdot \vec{a}_x = -\frac{\sqrt{3}}{2}k_X - \frac{3}{2}k_Y$;
- for $\vec{a} = \vec{a}_y = a_0(0, 1, 0) \rightarrow \vec{K} \cdot \vec{a}_y = \frac{\sqrt{3}}{2}k_X - \frac{3}{2}k_Y$;
- for $\vec{a} = \vec{a}_z = a_0(0, 0, 1) \rightarrow \vec{K} \cdot \vec{a}_z = 0$;

where the latter is zero due to the fact that the two atoms connected by \vec{a}_z are within the same elementary cell. We can evaluate the matrix elements appearing in Eq. 20 for the t_{2g} orbitals and thus obtain the following matrix elements connecting Ti_1 with Ti_2

$$\langle i_{\vec{k}}, \text{Ti}_1 | H_0 | j_{\vec{k}}, \text{Ti}_2 \rangle = \eta_p \frac{V_{pd\pi}(\sqrt{2})^{7/4}}{\sqrt{15}} \begin{pmatrix} 0 & -2ie^{i\frac{3}{2}k_Y} \sin(\frac{\sqrt{3}}{2}k_X) & 1 - e^{\frac{i}{2}(\sqrt{3}k_X+3k_Y)} \\ 2ie^{i3/2k_Y} \sin(\frac{\sqrt{3}}{2}k_X) & 0 & 1 - e^{-\frac{i}{2}(\sqrt{3}k_X-3k_Y)} \\ -1 + e^{\frac{i}{2}(\sqrt{3}k_X+3k_Y)} & -1 + e^{-\frac{i}{2}(\sqrt{3}k_X-3k_Y)} & 0 \end{pmatrix}, \quad (21)$$

where we expressed the matrix using the basis $\{|d_{yz}\rangle, |d_{zx}\rangle, |d_{xy}\rangle\}$ and introduced the Slater-Koster (SK) integral $V_{pd\pi}$. Let us now compute the next-to-nearest-neighbour terms (NNN), coupling the Ti atoms belonging to the same layer. In this case the direction which connects two different atoms, expressed in \vec{k} space, are:

- for $\vec{a} = \vec{a}_1 = a_0(0, +1, -1) \rightarrow \kappa_1 = -\frac{\sqrt{3}}{2}k_X + \frac{3}{2}k_Y$
- for $\vec{a} = \vec{a}_2 = a_0(-1, 0, +1) \rightarrow \kappa_2 = -\frac{\sqrt{3}}{2}k_X - \frac{3}{2}k_Y$;
- for $\vec{a} = \vec{a}_3 = a_0(+1, -1, 0) \rightarrow \kappa_3 = \sqrt{3}k_X$.

A straightforward calculation leads to two different matrices $H_{E\pi}$ and $H_{E\sigma}$ which are regulated by the two different SK parameters $V_{pd\pi}$ and $V_{pd\sigma}$ for the NNN contribution:

$$H_{E\pi} = \eta_p \frac{2i}{\sqrt{15}} V_{pd\pi} \begin{pmatrix} 0 & -(\sin(\kappa_1) + \sin(\kappa_2) + 2\sin(\kappa_3)) & (\sin(\kappa_1) + 2\sin(\kappa_2) + \sin(\kappa_3)) \\ (\sin(\kappa_1) + \sin(\kappa_2) + 2\sin(\kappa_3)) & 0 & -(2\sin(\kappa_1) + \sin(\kappa_2) + \sin(\kappa_3)) \\ (\sin(\kappa_1) + 2\sin(\kappa_2) + \sin(\kappa_3)) & (2\sin(\kappa_1) + \sin(\kappa_2) + \sin(\kappa_3)) & 0 \end{pmatrix} \quad (22)$$

$$H_{E\sigma} = \eta_p \frac{2i}{\sqrt{15}} \sqrt{3} V_{pd\sigma} \begin{pmatrix} 0 & (\sin(\kappa_1) + \sin(\kappa_2)) & -(\sin(\kappa_1) + \sin(\kappa_3)) \\ -(\sin(\kappa_1) + \sin(\kappa_2)) & 0 & (\sin(\kappa_2) + \sin(\kappa_3)) \\ (\sin(\kappa_1) + \sin(\kappa_3)) & -(\sin(\kappa_2) + \sin(\kappa_3)) & 0 \end{pmatrix}, \quad (23)$$

where we have neglected the spin and the layer degree of freedom, since it is diagonal in these labels. Referring to the approximation made by Ref. [22], we can use the form for the SK parameters

$$V_{pd\pi/\sigma} = n_{pd\pi/\sigma} \frac{\hbar^2 r_a^{3/2}}{m|a|^{7/2}} \quad (24)$$

where $r_a = 10.8$ nm, $\hbar^2/m = 7.62 \times 10^{-2}$ eV nm², $n_{pd\sigma} = -3.14$ and $n_{pd\pi} = 1.36$ and $|a|$ is the distance between the two atoms. Thus $V_{pd\pi} = 0.028$ eV and $V_{pd\sigma} = -0.065$ eV.

Furthermore since the magnitude of the electric field can be expressed via the electric potential between the two layers v as $|\vec{E}| = v\sqrt{3}/a_0$; $\eta_p \sim \frac{|\vec{E}|}{10 \text{ eV/nm}} \sim 0.09$ since $v = 0.2$ eV and $a_0 = 3.905$ nm.

Expansion for small fillings.

The previous expression is the full inversion symmetry breaking Hamiltonian, but it does not have the more common form of the Rashba interaction. We will perform another perturbation calculation in order to derive the usual expression of the Rashba term. We can evaluate exactly the eigenvectors of the first two dominant terms in the

complete Hamiltonian which are the TB Hamiltonian and the electrostatic contribution due to the local \vec{E} action on the states, which is denoted as $H_{\text{TB}} + H_{v0}$. Here we report H_{TB} in matrix form for simplicity²:

$$H_{\text{TB}} = \sum_{\vec{k}} \begin{pmatrix} d_{yz\text{Ti}_1, \vec{k}}^\dagger \\ d_{zx\text{Ti}_1, \vec{k}}^\dagger \\ d_{xy\text{Ti}_1, \vec{k}}^\dagger \\ d_{yz\text{Ti}_2, \vec{k}}^\dagger \\ d_{zx\text{Ti}_2, \vec{k}}^\dagger \\ d_{xy\text{Ti}_2, \vec{k}}^\dagger \end{pmatrix}^T \begin{pmatrix} 0 & 0 & 0 & \epsilon_{yz} & 0 & 0 \\ 0 & 0 & 0 & 0 & \epsilon_{zx} & 0 \\ 0 & 0 & 0 & 0 & 0 & \epsilon_{xy} \\ \epsilon_{yz}^* & 0 & 0 & 0 & 0 & 0 \\ 0 & \epsilon_{zx}^* & 0 & 0 & 0 & 0 \\ 0 & 0 & \epsilon_{xy}^* & 0 & 0 & 0 \end{pmatrix} \begin{pmatrix} d_{yz\text{Ti}_1, \vec{k}} \\ d_{zx\text{Ti}_1, \vec{k}} \\ d_{xy\text{Ti}_1, \vec{k}} \\ d_{yz\text{Ti}_2, \vec{k}} \\ d_{zx\text{Ti}_2, \vec{k}} \\ d_{xy\text{Ti}_2, \vec{k}} \end{pmatrix}, \quad (25)$$

where the interlayer contributions are:

$$\begin{aligned} \epsilon_{yz} &= -t_D \left(1 + e^{i(\frac{\sqrt{3}}{2}k_X - \frac{3}{2}k_Y)} \right) - t_I e^{-i(\frac{\sqrt{3}}{2}k_X + \frac{3}{2}k_Y)}, \\ \epsilon_{zx} &= -t_D \left(1 + e^{-i(\frac{\sqrt{3}}{2}k_X + \frac{3}{2}k_Y)} \right) - t_I e^{i(\frac{\sqrt{3}}{2}k_X - \frac{3}{2}k_Y)}, \\ \epsilon_{xy} &= -2t_D \cos\left(\frac{\sqrt{3}}{2}k_X\right) e^{-i\frac{3}{2}k_Y} - t_I, \end{aligned} \quad (26)$$

where $\vec{k} = k_X \hat{u}_{\text{T10}} + k_Y \hat{u}_{\text{T12}}$ is the dimensionless in-plane k vector of the Brillouin Zone. The whole matrix $H_{\text{TB}} + H_{v0}$, which is 12×12 , admits as eigenstates

$$|\psi_{i\sigma, \vec{k}}^\pm\rangle = \alpha_i(\vec{k}) e^{i\phi_i(\vec{k})} |d_{i1\sigma, k}\rangle + \beta_i^\pm(\vec{k}) |d_{i2\sigma, k}\rangle, \quad (27)$$

with

$$\begin{aligned} \alpha_i^\pm(\vec{k}) &= \frac{|\epsilon_i(\vec{k})|}{\sqrt{2|\epsilon_i(\vec{k})|^2 + \frac{v^2}{2} \pm v\sqrt{\frac{v^2}{4} + |\epsilon_i(\vec{k})|^2}}}; \\ \beta_i^\pm(\vec{k}) &= \frac{\left(\frac{v}{2} \pm \sqrt{\frac{v^2}{4} + |\epsilon_i(\vec{k})|^2}\right)}{\sqrt{2|\epsilon_i(\vec{k})|^2 + \frac{v^2}{2} \pm v\sqrt{\frac{v^2}{4} + |\epsilon_i(\vec{k})|^2}}}; \\ \phi_i(\vec{k}) &= \arg[\epsilon_i(\vec{k})] \end{aligned} \quad (28)$$

where the orbitals are labeled by the index i and the spin using the index σ . The corresponding eigenvalues are

$$\mathcal{E}_i^\pm(\vec{k}) = \pm \sqrt{\frac{v^2}{4} + |\epsilon_i(\vec{k})|^2}. \quad (29)$$

These states are well separated in six upper bands $|\psi_{i\sigma, k}^+\rangle$ and six lower bands $|\psi_{i\sigma, k}^-\rangle$. From now on we will take into account only the lower states, so we will neglect the \pm label.

The six lower bands are degenerate at the origin. Consequently, for sufficiently small values of \vec{k} , the TB hamiltonian splits the bands only by an amount of the order of $t_3|\vec{k}|^2$.

In order to obtain the Electric field Hamiltonian on the six lower bands for low fillings, we simultaneously linearize the Electric field Hamiltonians 22 and 23 as a function of \vec{k} and evaluate its matrix elements among the six lower states in Eq. 27, evaluated for $\vec{k} = 0$. The result is the following linear Hamiltonian:

$$(H_E)_{ij} = -i\mathcal{F}\epsilon_{ijk}\kappa_k, \quad \text{where} \quad \mathcal{F} = \frac{2\eta_p}{\sqrt{15}} \left(V_{pd\pi}(1 + 2^{7/8}\alpha\beta \cos(\phi)) + \sqrt{3}V_{pd\sigma} \right), \quad (30)$$

² The double spin degeneracy is understood.

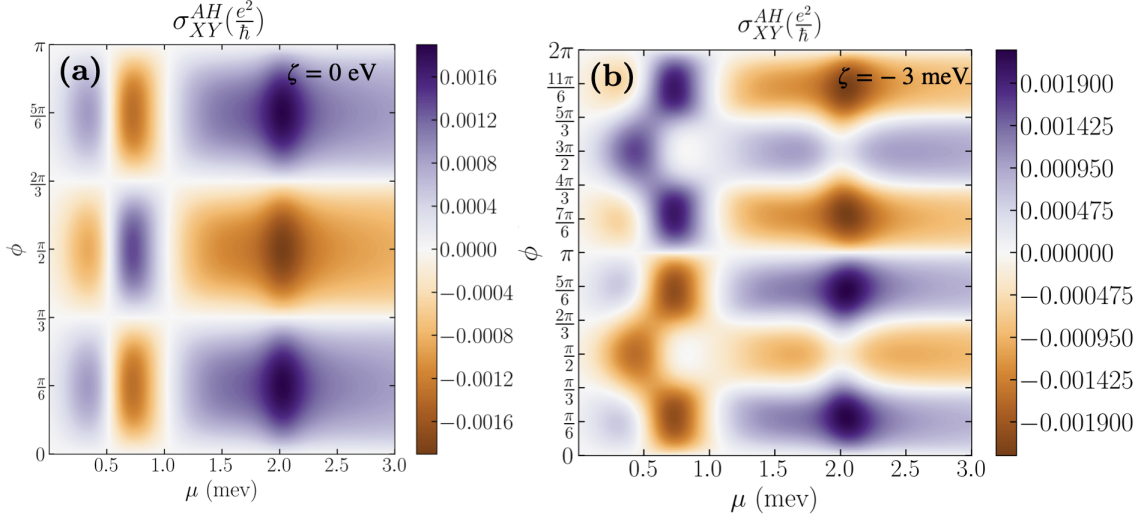


Figure 6. (a) Anomalous Hall conductivity as a function of μ for different values of ϕ at $|\vec{B}| = 5$ T and $T = 10$ K. The pattern is periodic with a change in sign of the conductivity for $\phi = n\pi/3$, with $n \in \mathbb{Z}$. (b) Anomalous Hall conductivity when \vec{B} is in-plane as a function of μ for different values of ϕ at $|\vec{B}| = 5$ T, $\zeta = -0.003$ eV and $T = 10$ K.

$\vec{\kappa} = (\kappa_1, \kappa_2, \kappa_3)$ as defined above and α, β and ϕ are the Eqs. 28 evaluated for $\vec{k} = 0$.

Identifying now the matrix elements of the orbital angular momentum \hat{L} matrices, we can rewrite this term as:

$$H_E = \frac{3}{\sqrt{2}} \mathcal{F}(\vec{k} \times \hat{L}) \cdot \frac{\vec{E}}{|\vec{E}|} \otimes \mathbb{1}_{\sigma\sigma'}. \quad (31)$$

This term has the same structure of the Rashba coupling, but it involves \hat{L} instead of \hat{S} ; this term is named orbital Rashba coupling [26]. The same coupling has been derived using another electrostatic argument [39–42]. Having introduced the notation of the angular momentum we can write also the reduced 6×6 matrix of the TB over the states 27 using the same notation:

$$H_{\text{TB}} = \sum_i \mathcal{E}_i (\mathbb{1} - L_i^2) \otimes \mathbb{1}_{\sigma\sigma'}, \quad (32)$$

where \mathcal{E}_i are the quadratic expansion of Eq. 29. Also H_{TRI} admits an expression of the form

$$H_{\text{TRI}} = \Delta (\mathbb{1} - \frac{3}{2} L_{111}^2). \quad (33)$$

Now, it is clear that, when \vec{k} is small enough that SOC is the dominant contribution, the previous couplings can be evaluated over the SOC eigenstates, and thus the total angular momentum appears leading to the Hamiltonian

$$H_{\text{eff}}(|\vec{k}| \sim 0) = -\tilde{\Delta} J_{111}^2 + \tilde{\mathcal{F}}(\vec{k} \times \hat{J}) + \sum_i \mathcal{E}_i(\vec{k}) (\nu \mathbb{1} - \tau J_i^2). \quad (34)$$

Appendix C TOTAL ANGULAR MOMENTUM PATTERN

In this section we report the in- and out-of-plane pattern of the total angular momentum \vec{J} for sake of completeness. The mean value of $|\vec{J}|$ saturates to its highest value for the first two doublets to $3/2\hbar$ while for the third one to $1/2\hbar$: which is another sign of the total angular momentum interpretation for the low energy doublets.

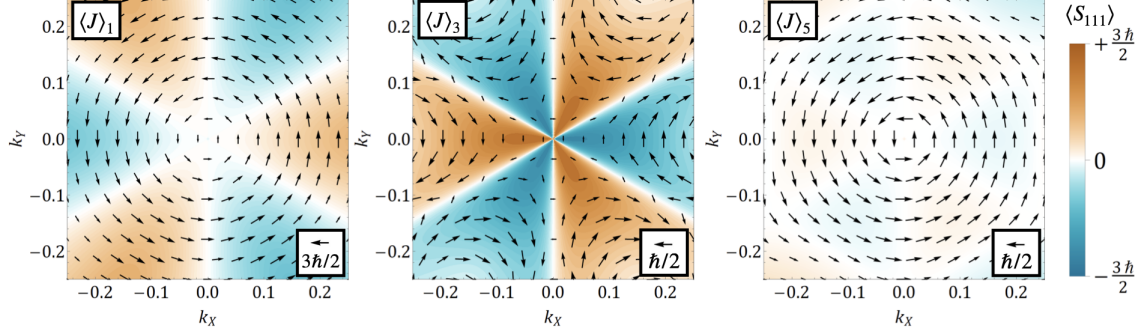


Figure 7. In- and out-of-plane spin and angular momentum modulation for the first and the third band. The second and the fourth are specular to the ones shown. The in-plane patterns are represented by the arrows and are obtained by computing the mean value of the spin components $J_{[\bar{1}10]}$ and the $J_{[\bar{1}\bar{1}2]}$ over the eigenstates of the chosen band. The colours indicate the modulation out-of-plane.

Appendix D BREAKING OF THE C_{3v} SYMMETRY: TETRAGONAL STRAIN

As we have shown in the main text, Fig. 6(a), which we report here for convenience, manifests the C_{3v} symmetry of the system. In figure we observe two different types of white line on which the conductance vanishes. The vertical lines represent the vanishing of the conductance for a fixed chemical potential, by varying the direction of the magnetic field. The zero conductance, for this value of the chemical potential, does not depend on the direction of \vec{B} since the shape of the Berry curvature is only rotated, while the energy splitting between the bands depends only on the magnitude of \vec{B} . The horizontal lines, instead, depends on an accidental residual degeneracy of the system and therefore the Berry curvature cannot be defined along these lines, leading to the vanishing of the conductance. The degeneracy we refer to is the reflection symmetry around \vec{B} on the $\Gamma\text{M}(\Gamma\text{M}')$ line when \vec{B} is aligned to the $\Gamma\text{K}(\Gamma\text{K}')$ line. This effect depends crucially on the C_{3v} symmetry of the system.

However, at low temperatures it is possible to have an additional tetragonal distortion which can be comparable in order of magnitude with the other couplings. This induces a tetragonal strain at the interface, resulting in the energetic preference of one orbital, e.g. the d_{xy} , with respect to the others. This term will reduce the symmetry of the lattice, changing the prediction we made. In order to take into account this distortion in the system one has to include the following Hamiltonian

$$H_z = \frac{\zeta}{2} \sum_{\vec{k}} \sum_{\alpha, \sigma} d_{xy \alpha \sigma, \vec{k}}^\dagger d_{xy \alpha \sigma, \vec{k}}, \quad (35)$$

where we choose $\zeta = -0.003$ eV. This term can be written with the angular momentum notation we used for the derivation of Eqs. 31, 32 and 33 by the same procedure

$$H_z = \frac{\zeta}{2} (\mathbb{1} - L_z^2). \quad (36)$$

This term can be further expressed in terms of the total angular momentum \vec{J} when the SOC is the dominant interaction, obtaining

$$H_z \sim \frac{\zeta}{3} J_z^2 + \text{const.} \quad (37)$$

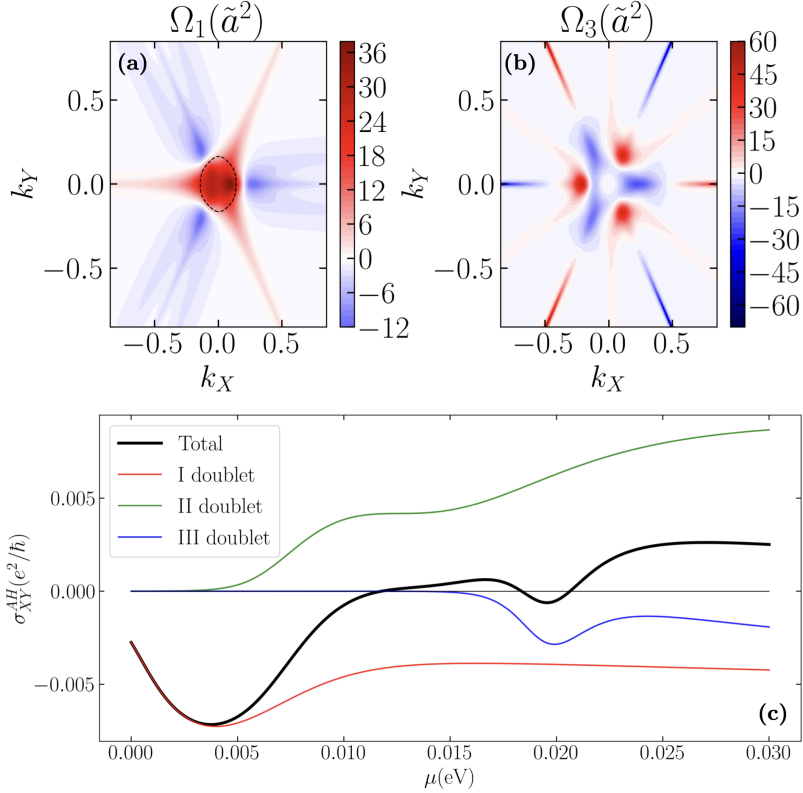


Figure 8. Berry curvatures for (a) the first and (b) the third band when the magnetic field is out-of-plane at $|\vec{B}| = 5$ T and $\zeta = -0.003$ eV. (c) Anomalous Hall conductance as a function of the chemical potential. The dashed line in (a) represents the Fermi surface at the dip of the conductance.

Since both J_z^2 and J_{111}^2 appear in the Hamiltonian, it is impossible to select a set of eigenstates which are also eigenstates of one of the component of \vec{J} .

When the out-of-plane magnetic field is included into the system the effect of the tetragonal strain is to modify the shape of the Berry curvature, reducing the symmetry of the system from C_{3v} to a in-plane reflection, as one can see in Fig 8(a). This has however small consequences on the anomalous Hall conductance for out-of-plane magnetic field, as one can observe in Fig. 8(c).

The most interesting effect is when \vec{B} is in-plane. The tetragonal strain generally removes the horizontal white lines in Fig. 6(a) except when the magnetic field is orthogonal to the direction of the in-plane projection of the strain direction. This behaviour is exemplified in Fig. 6(b) where $\sigma_{XY}^{AH} = 0$ only when $\phi = 0$ or π due to this symmetry protection.

Appendix E ROLE OF CORRELATIONS

The Hubbard Hamiltonian we take into account, written in real space, is the following

$$H_H = U \sum_{r,\alpha} n_{r\alpha\uparrow} n_{r\alpha\downarrow} + \frac{1}{2} \sum_{r,\alpha \neq \beta, \sigma \sigma'} (U' - J\delta_{\sigma\sigma'}) n_{r\alpha\sigma} n_{r\beta\sigma'}, \quad (38)$$

in which $n_{r\alpha\sigma}$ is the number operator of the state located in the site r occupying the orbital α with spin σ : we choose the basis spin states to be aligned (or antialigned) with the direction of the magnetic field. This choice is physically motivated by the observation that a spin imbalance in the Hamiltonian can only be generated by the magnetic field. We suppressed the label of the Ti atom due the local nature of the interaction (in other terms, r runs in the same time over the location of the elementary cell and the type of atom). Considering the Hamiltonian in the mean field

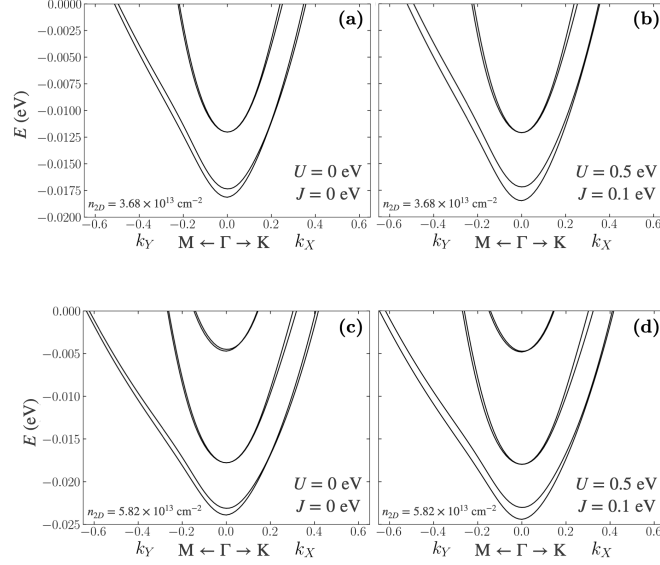


Figure 9. Electronic band structure evaluated for (a-c) $U = 0$ eV and $J = 0$ eV and (b-d) $U = 0.5$ eV and $J = 0.1$ eV with $B = 5$ T and $\phi = \pi/2$. $E = 0$ corresponds to the Fermi level when the 2D electron density is (a-b) $n_{2D} = 3.68 \times 10^{13} \text{ cm}^{-2}$ or (c-d) $n_{2D} = 5.82 \times 10^{13} \text{ cm}^{-2}$.

approximation we obtain, suppressing the index of the site r ,

$$H_H = \sum_{\alpha} n_{\alpha\uparrow} \left(U \langle n_{\alpha\downarrow} \rangle + \sum_{\beta \neq \alpha} (U' - J) \langle n_{\beta\uparrow} \rangle + U' \langle n_{\beta\downarrow} \rangle \right) + (\uparrow \leftrightarrow \downarrow). \quad (39)$$

Due to translational invariance H_H is local and can be written in \vec{k} space. By choosing $U' = U - 2J$ by rotational invariance [43], the Hamiltonian has only two free parameters. The band structure depends on the fillings, which are evaluated self-consistently. Our algorithm proceeds in the following way: in the absence of correlations we evaluate, for a fixed chemical potential, the electron occupations for each orbital $\langle n_{\alpha}^0 \rangle$ and the total occupation $N_0 = \sum_{\alpha} \langle n_{\alpha}^0 \rangle$. We include the correlations and we evaluate the bands using the $\langle n_{\alpha}^0 \rangle$. From this band structure we find the chemical potential at which the total density is equal to N_0 . We use $\langle n_{\alpha}^0 \rangle$ corresponding to this renormalized chemical potential as a starting point for a routine which self-consistently evaluates the correct filling fractions. The renormalized bands in the regime of small fillings considered in the paper are depicted in Fig. 9. The predicted AH conductivity for different choices of parameters is depicted in Fig. 10. The correlations do not change the non-linear behaviour of the conductivity, and their main effect is a renormalization of the magnetic field \vec{B} and the electric field v depending on the filling. When we reach the regime of $U = 0.5$ eV the behaviour of the third doublet changes showing a new dip and the curve does not change its sign anymore. This behaviour traces a new regime in the correlations which can significantly modify the conductance: this property could be exploited to test the strength of correlations in the (111) LAO/STO interface, a question which is still debated in literature. We notice that the values of U considered in this work are not large, but they are comparable with the electron bandwidth. Furthermore, in LAO/STO systems analyzed in this work, the typical particle densities are low compared to the half-filling regime. Accordingly, the net contribution to the total energy from Hubbard interaction is small. Furthermore, in these density regimes, the effects from polaron dynamics can be important on the electronic states [44] giving rise to a net lowering of the Hubbard interaction for the electronic system.

Appendix F TEMPERATURE ANALYSIS

The results we show in the paper are obtained by fixing the temperature at $T = 10$ K. However, they strongly depend on the temperature. For this reason we show in Fig. 11 the AH conductance for an in-plane magnetic ($\phi = \pi/2$)

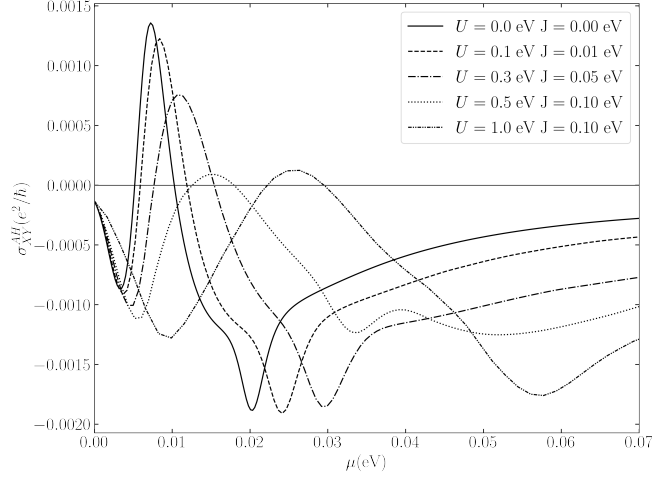


Figure 10. Anomalous Hall conductance as a function of the chemical potential fixing $|\vec{B}| = 5$ T and $\phi = \pi/2$ for different values of correlation parameters.

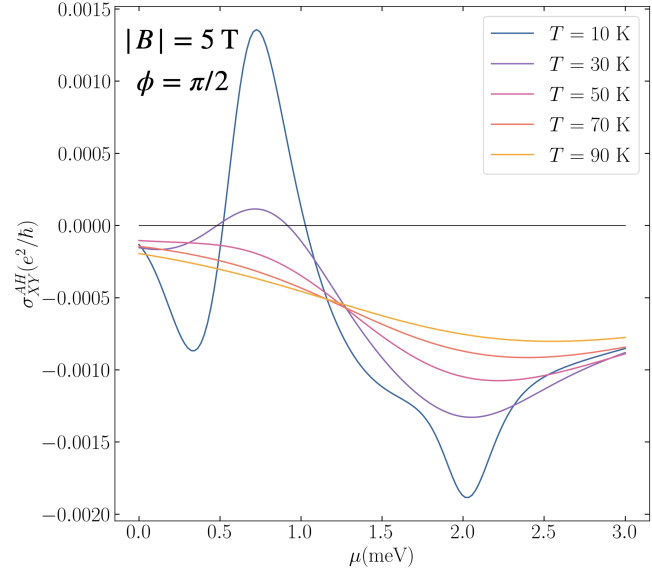


Figure 11. Anomalous Hall conductance as a function of the chemical potential fixing $|\vec{B}| = 5$ T and $\phi = \pi/2$ for different values of temperature T .

field at $B = 5$ T for different values of temperature. The picture shows that the non linear behaviour is still present, but the modulation is strongly suppressed by the temperature, since the ring contribution is no more present due to the smearing of the Fermi function. We point out that the role of temperature not only affects the Fermi function, but also the mobility of the bands and the scattering rate with impurities. These effects can overcome the intrinsic contribution we evaluated and make it more difficult to isolate it at higher temperatures.

-
- [1] Smit J. *Physica (Amsterdam)*, 21(1):877, 1955.
 [2] L. Berger. *Phys. Rev. B*, 2:4559, 1970.

- [3] Robert Karplus and J. M. Luttinger. Hall effect in ferromagnetics. *Phys. Rev.*, 95:1154–1160, Sep 1954.
- [4] Jinwu Ye, Yong Baek Kim, A. J. Millis, B. I. Shraiman, P. Majumdar, and Z. Tešanović. Berry phase theory of the anomalous hall effect: Application to colossal magnetoresistance manganites. *Phys. Rev. Lett.*, 83:3737–3740, Nov 1999.
- [5] Onoda M. and N. Nagaosa. Berry phase theory of the anomalous hall effect. *J. Phys. Soc. Jpn.*, 71:19, 2002.
- [6] Y. Lyanda-Geller, S. H. Chun, M. B. Salamon, P. M. Goldbart, P. D. Han, Y. Tomioka, A. Asamitsu, and Y. Tokura. Charge transport in manganites: Hopping conduction, the anomalous hall effect, and universal scaling. *Phys. Rev. B*, 63:184426, Apr 2001.
- [7] T. Jungwirth, Qian Niu, and A. H. MacDonald. Anomalous hall effect in ferromagnetic semiconductors. *Phys. Rev. Lett.*, 88:207208, May 2002.
- [8] Taguchi y. and et al. Berry phase theory of the anomalous hall effect. *Science.*, 291:2573, 2001.
- [9] Harold Y Hwang, Yoh Iwasa, Masashi Kawasaki, Bernhard Keimer, Naoto Nagaosa, and Yoshinori Tokura. Emergent phenomena at oxide interfaces. *Nature materials*, 11(2):103–113, 2012.
- [10] Stefano Gariglio, AD Caviglia, Jean-Marc Triscone, and M Gabay. A spin-orbit playground: Surfaces and interfaces of transition metal oxides. *Reports on Progress in Physics*, 82(1):012501, 2018.
- [11] A. D. Caviglia, M. Gabay, S. Gariglio, N. Reyren, C. Cancellieri, and J.-M. Triscone. Tunable rashba spin-orbit interaction at oxide interfaces. *Phys. Rev. Lett.*, 104:126803, 2010.
- [12] David Doennig, Warren E Pickett, and Rossitza Pentcheva. Massive Symmetry Breaking in $\text{LaAlO}_3/\text{SrTiO}_3$ (111) Quantum Wells: A Three-Orbital Strongly Correlated Generalization of Graphene. *Physical Review Letters*, 111(12):126804, 2013.
- [13] M. Trama, V. Cataudella, and C. A. Perroni. Strain-induced topological phase transition at (111) SrTiO_3 -based heterostructures. *Phys. Rev. Research*, 3:043038, Oct 2021.
- [14] AMRVL Monteiro, DJ Groenendijk, Inge Groen, Joeri de Bruijckere, Rocco Gaudenzi, HSJ Van Der Zant, and AD Caviglia. Two-dimensional superconductivity at the (111) $\text{LaAlO}_3/\text{SrTiO}_3$ interface. *Physical Review B*, 96(2):020504, 2017.
- [15] S Davis, Z Huang, K Han, T Venkatesan, V Chandrasekhar, et al. Magnetoresistance in the superconducting state at the (111) $\text{LaAlO}_3/\text{SrTiO}_3$ interface. *Physical Review B*, 96(13):134502, 2017.
- [16] Pan He, S. McKeown Walker, Steven S.-L. Zhang, F. Y. Bruno, M. S. Bahrany, Jong Min Lee, Rajagopalan Ramaswamy, Kaiming Cai, Olle Heinonen, Giovanni Vignale, F. Baumberger, and Hyunsoo Yang. Observation of Out-of-Plane Spin Texture in a SrTiO_3 (111) Two-Dimensional Electron Gas. *Phys. Rev. Lett.*, 120:266802, Jun 2018.
- [17] Felix Trier, Paul Noël, Joo-Von Kim, Jean-Philippe Attané, Laurent Vila, and Manuel Bibes. Oxide spin-orbitronics: spin-charge interconversion and topological spin textures, 2021.
- [18] Hans Keppler. *Crystal field theory*, pages 118–120. Springer Netherlands, Dordrecht, 1998.
- [19] M. Trama and al. Supplemental material.
- [20] Di Xiao, Wenguang Zhu, Ying Ran, Naoto Nagaosa, and Satoshi Okamoto. Interface engineering of quantum hall effects in digital transition metal oxide heterostructures. *Nature Communications*, 2(1):1–8, 2011.
- [21] AMRVL Monteiro, M Vivek, DJ Groenendijk, P Bruneel, I Leermakers, U Zeitler, M Gabay, and AD Caviglia. Band inversion driven by electronic correlations at the (111) $\text{LaAlO}_3/\text{SrTiO}_3$ interface. *Physical Review B*, 99(20):201102, 2019.
- [22] KV Shanavas, Zoran S Popović, and S Satpathy. Theoretical model for rashba spin-orbit interaction in d electrons. *Physical Review B*, 90(16):165108, 2014.
- [23] C. A. Perroni, H. Ishida, and A. Liebsch. Exact diagonalization dynamical mean-field theory for multiband materials: Effect of Coulomb correlations on the Fermi surface of $\text{Na}_{0.3}\text{CoO}_2$. *Phys. Rev. B*, 75:045125, 2007.
- [24] Yun-Yi Pai, Anthony Tylan-Tyler, Patrick Irvin, and Jeremy Levy. Physics of SrTiO_3 -based heterostructures and nanostructures: a review. *Reports on Progress in Physics*, 81(3):036503, 2018.
- [25] Pan He, S McKeown Walker, Steven S-L Zhang, Flavio Yair Bruno, MS Bahrany, Jong Min Lee, Rajagopalan Ramaswamy, Kaiming Cai, Olle Heinonen, Giovanni Vignale, et al. Observation of out-of-plane spin texture in a SrTiO_3 (111) two-dimensional electron gas. *Physical review letters*, 120(26):266802, 2018.
- [26] Dongwook Go, Daeyeun Jo, Hyun-Woo Lee, Mathias Kläui, and Yuriy Mokrousov. Orbitronics: Orbital currents in solids. 135(3):37001, aug 2021.
- [27] The reason is well explained by the effective model in Eq. 34 since $\vec{k} \times \hat{J}$ acts as a combination of ladder operator for \hat{J} . In fact, this doublet does not have direct transitions between $J_{111} = 3/2$ and $J_{111} = -3/2$ states. The Rashba splitting appears only in the third order of \vec{F} .
- [28] Naoto Nagaosa, Jairo Sinova, Shigeki Onoda, A. H. MacDonald, and N. P. Ong. Anomalous hall effect. *Rev. Mod. Phys.*, 82:1539–1592, May 2010.
- [29] T. Miyasato, N. Abe, T. Fujii, A. Asamitsu, S. Onoda, Y. Onose, N. Nagaosa, and Y. Tokura. Crossover behavior of the anomalous hall effect and anomalous nernst effect in itinerant ferromagnets. *Phys. Rev. Lett.*, 99:086602, Aug 2007.
- [30] Athby H Al-Tawhid, Jesse Kanter, Mehdi Hatefipour, Douglas L Irving, Divine P Kumah, Javad Shabani, and Kaveh Ahadi. Oxygen vacancy-induced anomalous hall effect in a non-magnetic oxide. *arXiv preprint arXiv:2109.08073*, 2021.
- [31] G. Mattoni, D. J. Baek, N. Manca, N. Verhagen, D. J. Groenendijk, L. F. Kourkoutis, A. Filippetti, and A. D. Caviglia. Insulator-to-Metal Transition at Oxide Interfaces Induced by WO_3 Overlayers. *ACS Appl. Mater. Interfaces*, 9:42336–42343, 2017.
- [32] Sumanta Tewari, Snehasish Nandy, Girish Sharma, and Arghya Taraphder. Chiral anomaly as origin of planar Hall effect in Weyl semimetals. In *APS March Meeting Abstracts*, volume 2018 of *APS Meeting Abstracts*, page F40.002, January 2018.
- [33] C. A. Perroni, V. Cataudella, M. Salluzzo, M. Cuoco, and R. Citro. Evolution of topological superconductivity by orbital-selective confinement in oxide nanowires. *Phys. Rev. B*, 100:094526, 2019.

- [34] L. Lepori, D. Giuliano, A. Nava, and C. A. Perroni. Interplay between singlet and triplet pairings in multiband two-dimensional oxide superconductors. *Phys. Rev. B*, 104:134509, 2021.
- [35] Flavio Y Bruno, Siobhan McKeown Walker, Sara Riccò, Alberto De La Torre, Zhiming Wang, Anna Tamai, Timur K Kim, Moritz Hoesch, Mohammad S Bahramy, and Felix Baumberger. Band Structure and Spin–Orbital Texture of the (111)-KTaO₃ 2D Electron Gas. *Advanced Electronic Materials*, 5(5):1800860, 2019.
- [36] Edouard Lesne, Yildiz G Sağlam, Raffaele Battilomo, Thierry C van Thiel, Ulderico Filippozzi, Mario Cuoco, Gary A Steele, Carmine Ortix, and Andrea D Caviglia. Designing berry curvature dipoles and the quantum nonlinear hall effect at oxide interfaces. *arXiv preprint arXiv:2201.12161*, 2022.
- [37] Daniel Khomskii. *Transition metal compounds*. Cambridge University Press, 2014.
- [38] GM De Luca, R Di Capua, E Di Gennaro, A Sambri, F Miletto Granozio, G Ghiringhelli, D Betto, C Piamonteze, NB Brookes, and M Salluzzo. Symmetry breaking at the (111) interfaces of SrTiO₃ hosting a two-dimensional electron system. *Physical Review B*, 98(11):115143, 2018.
- [39] Seung Ryong Park, Choong H Kim, Jaejun Yu, Jung Hoon Han, and Changyoung Kim. Orbital-angular-momentum based origin of rashba-type surface band splitting. *Physical review letters*, 107(15):156803, 2011.
- [40] Beomyoung Kim, Panjin Kim, Wonsig Jung, Yeongkwan Kim, Yoonyoung Koh, Wonshik Kyung, Joonbum Park, Masaharu Matsunami, Shin-ichi Kimura, Jun Sung Kim, et al. Microscopic mechanism for asymmetric charge distribution in rashba-type surface states and the origin of the energy splitting scale. *Physical Review B*, 88(20):205408, 2013.
- [41] Panjin Kim, Kyeong Tae Kang, Gyungchoon Go, and Jung Hoon Han. Nature of orbital and spin Rashba coupling in the surface bands of SrTiO₃ and KTaO₃. *Physical Review B*, 90(20):205423, 2014.
- [42] Jisook Hong, Jun-Won Rhim, Changyoung Kim, Seung Ryong Park, and Ji Hoon Shim. Quantitative analysis on electric dipole energy in rashba band splitting. *Scientific reports*, 5(1):1–9, 2015.
- [43] Antoine Georges, Luca de’ Medici, and Jernej Mravlje. Strong correlations from hund’s coupling. *Annu. Rev. Condens. Matter Phys.*, 4(1):137–178, 2013.
- [44] C. A. Perroni, G. De Filippis, and V. Cataudella. Ground-state features and spectral properties of large polaron liquids from low to high charge densities. *Phys. Rev. B*, 103:245130, 2021.